This is a preprint, the final version is subject to change, of the American Mineralogist (MSA)
Cite as Authors (Year) Title. American Mineralogist, in press.
DOI: https://doi.org/10.2138/am-2019-6969

Revision 2

Chemical and textural relations of britholite- and apatite-group minerals from hydrothermal REE mineralization at the Rodeo de los Molles deposit, Central Argentina

Authors:

Melanie Lorenz[1], Uwe Altenberger[1], Robert B. Trumbull[2], Raúl Lira[3], Mónica López de Luchi[4], Christina Günter[1], Sascha Eidner[5]

Affiliation(s):

1: Institute of Geosciences, University of Potsdam, Karl-Liebknecht-Str. 24-25, 14476 Potsdam, Germany

2: GFZ German Research Centre for Geosciences, Telegrafenberg, 14473 Potsdam, Germany

3: CONICET – Museo de Mineralogía y Geología "Dr. A. Stelzner", Facultad de Ciencias Exactas, Físicas y Naturales, University of Córdoba, Av. Velez Sarsfield 299, X5000JJC Córdoba, Argentina

4: IGNEIS - Instituto de Geocronología y Geología Isotópica, CONICET – University of Buenos Aires, Pabellón Igneis - Ciudad Universitaria, C1428EHA Buenos Aires, Argentina

5: Institute of Chemistry (Physical Chemistry), University of Potsdam, Karl-Liebknecht-Str. 24-25, 14476 Potsdam, Germany

E-mail address of corresponding author:

Melanie Lorenz: melloren@uni-potsdam.de

E-mail address of co-authors:

Uwe Altenberger: altenber@uni-potsdam.de

Robert B. Trumbull: bobby@gfz-potsdam.de

Raúl Lira: raul.lira@unc.edu.ar

Mónica López de Luchi: deluchi@ingeis.uba.ar

Christina Günter: Christina.Guenter@geo.uni-potsdam.de

Sascha Eidner: eidner@chem.uni-potsdam.de

Abstract

Britholite group minerals $(REE,Ca)_5[(Si,P)O_4]_3(OH,F)$ are rather widespread rare-earth minerals in alkaline rocks and their associated metasomatic zones, where they usually are minor accessory phases. An exception is the REE deposit Rodeo de los Molles, Central Argentina, where fluorbritholite-(Ce) (FBri) is the main carrier of REE and is closely intergrown with fluorapatite (FAp). These minerals reach an abundance of locally up to 75 modal % (FBri) and 20 modal % (FAp) in the vein mineralizations. The Rodeo de los Molles deposit is hosted by a fenitized monzogranite of the Middle Devonian Las Chacras-Potrerillos batholith. The REE mineralization consists of fluorbritholite-(Ce), britholite-(Ce), fluorapatite, allanite-(Ce), and REE fluorcarbonates, and is associated with hydrothermal fluorite, quartz, albite, zircon, and titanite. The REE assemblage takes two forms: irregular patchy shaped REE-rich composites and discrete cross-cutting veins. The are more common, but here fluorbritholite-(Ce) is mostly replaced by REE carbonates. The vein mineralization has more abundant and better preserved britholite phases.

The majority of britholite grains at are hydrothermally altered, and alteration is strongly enhanced by metamictization, which is indicated by darkening of the mineral, loss of birefringence, porosity and volume changes leading to polygonal cracks in and around altered grains. A detailed electron microprobe study of apatite-britholite minerals from Rodeo de los Molles revealed compositional variations in fluorapatite and fluorbritholite-(Ce) consistent with the coupled substitution of $REE^{3+} + Si^{4+} = Ca^{2+} + P^{5+}$ and a compositional gap of ~4 apfu between the two phases, which we interpret as a miscibility gap. Micron-scale intergrowths of fluorapatite in fluorbritholite-(Ce) minerals and vice versa are documented here for the first time and interpreted as exsolution textures that formed during cooling below the proposed solvus.

Keywords: Britholite, apatite, exsolution textures, miscibility gap, compositional gap, REE, fenite, alkaline granites, hydrothermal alteration

Introduction

The britholite group minerals are members of the apatite supergroup and have the general formula $(REE,Ca)_5[(Si,P)O_4]_3(OH,F)$ (Pasero et al. 2010). Winther (1901) was the first to describe the mineral group, in nepheline syenites from the Ilimaussaq complex, SW Greenland. Since then, britholite minerals have been identified in alkaline and felsic magmatic rocks and associated metasomatic zones in many other parts of the world (e.g., Nash 1972; Arden and Halden 1999; Della Ventura et al. 1999; Macdonald et al. 2013; Uher et al. 2015; Melluso et al. 2017; Zozulya et al. 2015, 2017). Occurrences have also been described in carbonatites (Ouzegane et al. 1988; Ahijado et al. 2005; Torró et al. 2012), potassic volcanic rocks (Orlandi et al. 1989), iron skarn deposits (Holtstam and Andersson 2007), and in copper ores (Brugger et al. 2006; Ferguson et al. 2016). Thus, britholite minerals are rather widespread rare-earth minerals, so it is surprising that few analyses of their chemical composition have been published (e.g. Arden and Halden 1999; Lira et al. 1999; Uher et al. 2015; Zozulya et al. 2015, 2017). Even fewer studies have addressed their potential as REE ore minerals (Zozulya et al. 2015); possibly because britholite typically is a minor accessory phase. The britholite occurrence described in this paper is an exception.

In the 1980's an unusual REE occurrence with britholite as the major phase was discovered in the San Luis province of Argentina during follow-up of an aerial radiometric anomaly (Gay and Lira 1984). Further studies of the so-called Rodeo de los Molles deposit followed (Lira and Ripley 1990, 1992; Lira et al. 1999), and form the background for the detailed work reported here. The Rodeo de los Molles deposit occurs in a fenitized zone in the northern Las Chacras-Potrerillos batholith in central Argentina (Fig. 1). REE mineralization at Rodeo de los Molles mainly consists of fluorbritholite-(Ce) + fluorapatite + allanite-(Ce) + REE fluorcarbonates. Previous studies have described the form of the mineralized bodies and their main mineral assemblages (Lira and Ripley (1990, 1991, 1992), whom also presented results of fluid inclusion studies and stable isotope ratios in associated fluorite.

In this contribution, we present the results of a detailed petrographic and electron microprobe (EMP) study of britholite-group and associated apatite-group minerals at Rodeo de los Molles. A particular question addressed in this paper is the degree of solid solution between fluorapatite and fluorbritholite-(Ce). Another focus is on the low-temperature alteration and replacement textures of the britholite minerals, which is pervasive in this locality. The study of britholite alteration could be important in the context of radioactive waste management. This is because britholite minerals are natural analogues of synthetic rare earth silicates and actinides with an apatite structure, which are used for the solidification of liquid nuclear high-level waste (Livshits 2006).

The britholite group

Britholites are commonly hexagonal with space group $P6_3/m$ or $P6_3$ and typically contain significant contents of actinides (mainly U,Th) that cause metamictization. There are two natural end-members, britholite-(Ce) and britholite-(Y), which were formerly known as lessingite and abukumalite, respectively (Oberti et al. 2001). The britholite group currently contains seven members accepted by the International Mineralogical Association: britholite-(Ce), britholite-(Y), fluorbritholite-(Ce), fluorcalciobritholite, melanocerite-(Ce), tritomite-(Ce) and tritomite-(Y) (Pasero et al. 2010). The two relevant to this study are britholite-(Ce) and fluorbritholite-(Ce). Britholite-(Ce) is the most common member of the mineral group and is often used synonymously for the entire group. Fluorbritholite-(Ce) was first described by Gu et al. (1994) from Mont Saint-Hilaire, Québec, Canada, where it occurs as tan-colored needles in vugs, which probably formed during late magmatic and metasomatic stages. Fluorbritholite-(Ce) is the main ore-forming mineral in the mineralized pegmatitic nepheline syenite of the Sakharjok massif, Kola Peninsula, NW Russia (Zozulya et al. 2017), where it forms large (up to 1 cm) anhedral grains with a heterogeneous internal texture.

Geological background

The Rodeo de los Molles deposit is hosted by a biotite monzogranite of the Las Huertitas stock, which is part of the Middle Devonian Las Chacras-Potrerillos Batholith. The batholith consists of a nested set of six granitic intrusions (Fig. 1A; Siegesmund et al. 2004; López de Luchi et al. 2017). It owes its location to the intersection of two sinistral shear zones that produce a NNE-SSW extension, allowing the pulsed emplacement of successive magma batches. The timing of the different granites emplacements within the batholith is not well constrained. Two U-Pb ages of titanite and zircon suggest emplacement at 379 Ma (GPG) to 382 Ma (BPG), whereas 6 K-Ar mineral dates (for PG, EG, GPG, BPG) indicate (cooling) ages of 381 to 342 Ma (Siegesmund et al. 2004). The intrusion hosting the Rodeo de los Molles deposit (EG – equigranular granite) and the REE mineralization itself have been dated recently by U-Pb, giving ages of 369 ± 4 Ma (U-Pb on zircons) and 336 ± 29 Ma (U-Pb on fluorapatites), respectively (Lorenz et al. unpublished information).

REE mineralization at Rodeo de los Molles

The Rodeo de los Molles REE mineralization occurs within an elliptical zone of hydrothermally altered granite (fenite), which is an elongated area with a NNE-SSW orientation and about 2 km long and 600 m wide (Fig. 1B). The modal composition of the fenite varies from that of an alkali-feldspar quartz syenite to alkali-feldspar syenite (Lira et al. 1999). The REE mineralization takes two different forms in the fenite rocks: discrete cross-cutting veins (Fig. 2A,B,D) and irregular-shaped REE-rich mineral composites (Fig. 2C). The patchy REE-rich composites are scattered irregularly throughout the metasomatic zone (fenite) and are the more common REE- mineralized feature of the Rodeo de los Molles area, although the veins are of higher fluorbritholite-(Ce) concentration grade. The primary REE mineralization, in both forms, is characterized by an assemblage of fluorbritholite-(Ce) and fluorapatite, which are associated with britholite-(Ce), allanite-(Ce), zircon, titanite, fluorite,

feldspar and quartz. Aegirine-augite and phlogopite are also paragenetically associated, as they are always present in the REE mineralized areas (Lira and Ripley 1990). The mineralized veins reach up to 40 cm in thickness and contain exceptional abundances of fluorbritholite-(Ce), locally up to 75 modal %, and fluorapatite up to 20 modal %. Britholite-(Ce) only occurs as an alteration phase of fluorbritholite-(Ce). Figure 2 (B+D) shows a typical example of a mineralized vein in fenite with an albite-rich reaction zone at the contact (transition zone, TZ). Within the patchy REE-rich composites secondary REE fluorcarbonates replace fluorbritholite-(Ce) phases, but not fluorapatites. Since the veins have not been observed to intersect patches, it is unknown if these two features formed together or sequentially. However, late fluorite-calcite-REE-fluorcarbonate veins cut across the primary REE mineralization structures (Lira et al. 1999).

Samples and methods

The samples studied here were collected from one of the main fluorbritholite-(Ce) rich veins and the mineralized areas around it. Analyses for britholite and associated apatite mineral chemistry were done mainly on a drill-core sample (RDLM18) that shows the contact zone of the vein with the surrounding fenite (Fig. 2B+D). Another drill-core sample from the same vein was selected to cover the whole rock compositional range.

Petrographic observations of polished thin sections were made by polarized optical microscopy, which was supported by analyses with a JEOL JSM-6510 scanning electron microscope (SEM), equipped with an Oxford instrument EDS analyzer at the Institute of Earth- and Environmental Science, University of Potsdam.

Chemical analyses were carried out on a JEOL JXA-8200 electron microprobe (EMP) at the University of Potsdam. The conditions used for the analysis were 20kV acceleration voltage, 40 nA beam current and beam sizes between 2 µm and 20 µm. Counting times were between 10 s to 25 s on peak for major elements and 50 s for REE and other trace elements,

respectively. The following spectral lines and mainly Smithsonian natural mineral standards were used: fluorapatite (F Kα, P Kα, Ca Kα), albite (Na Kα), fayalite (Fe Kα, Mn Kα), wollastonite (Si Kα), omphacite (Al Kα), $LaPO_4$ (La Lα), $PrPO_4$ (Pr Lβ), $CePO_4$ (Ce Lα), $NdPO_4$ (Nd Lβ), YPO_4 (Y Lα), $EuPO_4$ (Eu Lα), $SmPO_4$ (Sm Lβ), $LuPO_4$ (Lu Lα), $GdPO_4$ (Gd Lα), $ErPO_4$ (Er Lβ), $DyPO_4$ (Dy Lβ), $YbPO_4$ (Yb Lα), $HoPO_4$ (Ho Lβ), monazite (Th Mα, U Mβ, Tb Lα), uranothorite (U Mβ), crocoite (Pb Mβ). Fluorine, as on of the least-stable components in apatite, was measured first during the analytical scheme. In order to reduce halogen migration, counting times for F were reduced to 6 s on peaks and 3 s on backgrounds. The EMPA data were reduced using the PRZ-XXP correction routine. Chemical formulae for britholite- and apatite-group minerals were calculated on the basis of 13 oxygens and 8 cations. The OH content was calculated from the relationship OH = 1 – (F+Cl), by assuming charge balance in apatite. Several qualitative EMP analyses showed chlorine contents below the detection limit and therefore Cl was set to 0 for the OH calculations. Representative EMPA data for fluorbritholites-(Ce) and fluorapatites are given in Table 1 and 2, respectively.

Raman spectroscopic measurements were carried out at the University of Potsdam, with a Witec alpha 300 Raman microscope using a 50x objective. A 532 nm Nd:YAG laser was used as an excitation source. The Raman spectra of the mineral surface were collected by screening areas of sizes 25 μm × 25 μm. All measured spectra were collected and analyzed using a parallel factor analyzing approach called PARAFAC, which was initially formulated by Harshman (1970) and Carroll and Chang (1970). Using this approach, a decomposition of measured spectra into single component spectra is possible, and hence, a recalculation of the distribution of the different components (minerals) in the sample.

Petrography

Britholite

Fluorbritholite-(Ce) is the primary britholite group mineral present and unusually abundant at Rodeo de los Molles. Based on optical estimates from thin-section petrography, it comprises up to 75 modal % of the REE vein mineralization. In contrast, it reaches only 5 modal % in the disseminated REE mineralization (REE-composites). In this setting, the mineral is mostly altered to REE fluorcarbonates. In vein mineralizations, britholite-(Ce) is a common alteration phase. Fluorbritholite-(Ce) generally forms single crystals and massive aggregates, which are typically intergrown with fluorapatite (Fig. 3; Gay and Lira 1984). Euhedral crystals of fluorbritholite-(Ce) are best preserved in vein structures within aggregates of titanite and hydrothermal zircon. The latter is characterized by low totals and a disturbed internal texture (Fig. 3A+B). Individual fluorbritholite-(Ce) grains range in size from a few micrometers up to one millimeter in length. Similarly large britholite group crystals have been described from the Vico Volcanic complex in Italy (britholite-(Ce); Della Ventura et al. 1999), and from the Eden Lake complex in Canada (britholite-(Ce); Arden and Halden 1999). At Rodeo de los Molles, fluorbritholite-(Ce) is typically enclosed in an albite + quartz ± K-feldspar-rich matrix. Crystals of fluorapatite, quartz, albite, K-feldspar, fluorite and tiny grains of an unidentified U-Th-Pb phase are found as inclusions within some of the grains. In veins, fluorbritholite-(Ce) has subhedral to anhedral crystal shapes. In plane-polarized light, it is weakly pleochroic from yellowish, light orange to light brown. In zones of strong alteration, the minerals become relatively dark grey-brown and the birefringence approaches zero. Both fresh and altered grains have a heterogeneous internal texture, with patchy discontinuous compositional patterns rather than regular zoning (Fig. 3A-D).

In the Rodeo de los Molles vein mineralization, we observed complex and mutual intergrowth textures of fluorbritholite-(Ce) and fluorapatite, which have not been described before (Fig. 3A-D; Supplementary Fig. 1+2). Overall, two types are recognizable. Type 1 are

intergrowth textures with fluorapatite (solute) inclusions within fluorbritholite-(Ce) host minerals. They have been found in euhedral inclusions of fluorbritholite-(Ce) within zircon (Fig. 3A), titanite (Fig. 3B), and also in discrete fluorbritholite-(Ce) aggregates (Fig. 3D). The second textural type is characterized by blebs of fluorbritholite-(Ce) in large fluorapatite host grains. In both cases the bleb- or worm-like textures are complex, show mostly no shape-preferred orientation and are relatively random (Fig. 3A,B+D; Supplementary Fig. 1A+B). In form, they resemble symplectites, but arguments are given in the discussion that they are not reaction textures but formed by unmixing. In the second type, the fluorbritholite-(Ce) blebs are sometimes oriented (Fig. 3C; Supplementary Fig. 1C+D).

Fluorbritholite-(Ce) shows significant post-crystallization alteration with domains of irregular shape and structure. Alteration affects crystal rims and typically penetrates significantly into the grains, leaving only small domains of primary (atoll-like) fluorbritholite-(Ce). Commonly, more than one alteration "front" is apparent. Grains with severe alteration are resorbed and have a high grade of porosity. These porous areas are unstable under the EMP, making good analyses impossible. Furthermore, many grains of fluorbritholite-(Ce) are pervasively cracked, with a distinctive polygonal pattern that resemble dessication cracks in mud. Polygonal cracking indicates a reduction in volume and is restricted to the altered regions. The interstitial grains of fluorapatite do not seem to be affected by this kind of alteration. Spatially associated minerals are either not fractured at all or they show a parallel arrangement of fractures. Zozulya et al. (2015) observed similar alteration features in britholite group minerals from the Sakharjok Zr-Y-REE deposit, Kola Peninsula, NW Russia.

Apatite

Overall, fluorapatite is closely intergrown with fluorbritholite-(Ce). Together they form aggregates that reach several centimeters in size. The contacts between the two phases are always sharp. Fluorapatite mostly occurs as small aggregates of anhedral grains on the order

of < 100µm across. These small, anhedral fluorapatites are inclusion-free and unzoned (FAp in Fig. 3). Even where they are included in highly resorbed and altered fluorbritholite-(Ce) crystals; fluorapatites do not show any sign of alteration. A separate generation of fluorapatite, with larger (up to 700 µm) anhedral to subhedral grains, is intergrown with the REE-rich composites and commonly surrounded by allanite-(Ce) (FAp-a in Fig. 3E+F). This generation occurs mostly euhedral and reaches sizes of up to 1 cm in length (FAp-a in Fig. 3E+F). They commonly contain inclusions of former fluorbritholite-(Ce) (now mostly replaced by REE fluorcarbonates) and some quartz.

In addition, there are interesting and variable textural relations of allanite-(Ce) with fluorapatite and fluorbritholite-(Ce). In the REE composite structures, allanite-(Ce) invariably forms rims around fluorapatite-fluorbritholite-(Ce) aggregates, whereas allanite-(Ce) rims are rare in the vein structures. The contact between allanite-(Ce) and the REE-rich composite assemblage (REE fluorcarbonate + fluorapatite + fluorbritholite-(Ce) ± fluorite ± quartz) is characterized by irregular embayments. Locally, another generation of fluorapatite occurs within the allanite-(Ce) rims of REE-rich composites. This fluorapatite can be distinguished by its euhedral to subhedral shape, straight edges, lack of inclusions, and sizes between 50 µm and 200 µm (FAp-b in Fig. 3F).

Mineral composition

Britholite

Alteration of fluorbritholite-(Ce) is very common at Rodeo de los Molles and has a strong effect on the mineral composition. The analyses of the fluorbritholite-(Ce) minerals show (0.4-2.2 apfu) Ca and (5.1-8.4 apfu) total REE in the M-site (Table 1). The highest Ca and the lowest REE contents are found in relatively unaltered relict “atoll” fluorbritholite-(Ce) (e.g. Fig. 3C) in the transition zone between the fenite and the vein mineralization, whereas the altered fluorbritholite-(Ce) in the same zone contain the highest REE and lowest Ca contents.

The T-site is dominated by Si, with 2.0 apfu in altered fluorbritholite-(Ce) within the transition zone and the REE composites. The highest Si concentrations are 3.8 apfu, representing near end member compositions, which were found in grains within the vein mineralization. Phosphorus contents are overall low (0.23 - 0.75 apfu). The ThO_2 values range between 0.49 wt.% and 2.19 wt.% (0.01 to 0.07 apfu) and UO_2 reaches 1.32 wt.% (0.04 apfu). The MnO content of unaltered fluorbritholite-(Ce) is up to 0.35 wt.% and can reach about twice that value (0.63 wt.%) in altered grains (Table 1). The EMP analyses of REE are incomplete, because the concentrations of Tb, Ho, Er, Tm, Yb, and Lu, especially in fluorapatite, were at or below the EMP detection limit (Table 1 and 2). Unfortunately, homogenous areas of fluorbritholite-(Ce) were too small and the mineral itself to instable for LA-ICP-MS measurements. Despite this limitation, the REE patterns of fluorbritholite-(Ce) and fluorapatite are parallel and differ by a factor of ~50 (Fig. 6). Both phases show a strong LREE enrichment relative to HREE, whereby fluorbritholite-(Ce) displays steeper patterns than fluorapatite (Ce/Y_{CN} = 30-54 vs. 11-38, respectively, where CN indicates chondrite-normalized). The Y contents are relatively constant (Table 1 and 2). Fluorbritholite-(Ce) and fluorapatite exhibit negative Eu anomalies, which are interpreted as primary features, since they occur in all generations, and are also represented by the host rock. Also, the REE patterns from Rodeo de los Molles are similar to those reported in studies of Macdonald et al. (2013) and Arden and Halden (1999) (Fig. 6). The EMP analyses of unaltered fluorbritholite-(Ce) show significantly higher oxide wt.% totals than those of altered fluorbritholite-(Ce), suggesting the presence of volatiles in the latter. This is supported by petrographic observations of higher porosity in phases with strong alteration. Analysis of a bulk sample from the fluorbritholite-(Ce)-rich vein yielded about 3.63 wt.% H_2O. Stoichiometric calculated H_2O for fluorbritholite-(Ce) ranges between 0 and 0.6 wt.% (Table 1). At Rodeo de los Molles most of the britholite-group phases have F > 0.5 apfu in the X-site classifying them as fluorbritholite-(Ce) (Fig. 4). Overall, the F content decreases with increasing alteration,

whereby highly altered grains with polygonal fractures show F < 0.5 apfu, classifying them as britholite-(Ce). The highest F contents, up to 1.4 apfu, are found in unaltered atoll fluorbritholite-(Ce). Here, F occurs in excess of the ideal stoichiometry (F = 1 apfu). Piccoli and Candela (2002) explained the phenomenon of excess F in apatites by the presence of significant amounts of CO_3^{2-}. In general, the carbonate ion can substitute either into the c-axis anion channel (X-site) or for the phosphate ion at the T-site of the britholite structure (Pan and Fleet 2002). One of the decomposed Raman spectra of altered fluorbritholite-(Ce) phases with replacement textures is shown in Figure 5 and corresponds best with REE-fluorcarbonates from the RRUFF-database, indicating the presence of CO_3^{2-} (Lafuente et al. 2015). The Raman spectra shows characteristic CO_3^{2-} vibrational modes (Frost and Dickfos 2007).

Apatite

In fluorapatites of Rodeo de los Molles, the M-site contains variable Ca (4.6-5.2 apfu) and REE (0.19-0.74 apfu; Table 2) values, which have a negative correlation. The T-site is occupied by P (2.6-2.9 apfu) and Si (0.1-0.3 apfu); S is negligible (< 0.1 apfu). The X-site is dominated by F (0.7-0.9 apfu), which led to their classification as fluorapatites (Fig. 4). The highest F concentrations are reached in fluorapatite inclusions within euhedral fluorbritholite-(Ce) crystals in hydrothermal zircon (exsolution type 1). The lowest F values are present in large fluorapatites within the transition zone (TZ) between the vein mineralization and the surrounding fenite (Fig. 2B). Fluorapatite crystals are overall unzoned, except for a patchy variation in the BSE intensity shown by some large fluorapatites grains (Fig. 3C). In general, Sr is one of the most common substituents for Ca in the apatite supergroup (Rakovan and Hughes 2000). Fluorapatites at Rodeo de los Molles contain up to 1.13 wt.% SrO, whereas Sr was below the detection limit for fluorbritholite-(Ce) analyses. Interestingly, SrO concentrations in fluorapatites are twice as high in the vein mineralizations as in the REE composites (1.13 wt.% and 0.49 wt.%, respectively).

This is a preprint, the final version is subject to change, of the American Mineralogist (MSA)
Cite as Authors (Year) Title. American Mineralogist, in press.
DOI: https://doi.org/10.2138/am-2019-6969

Discussion

Geochemical variations of the britholite group minerals

Previous studies (e.g. Rønsbo 1989; Arden and Halden 1999; Macdonald et al. 2013; Uher et al. 2015; Zozulya, et al. 2017) have demonstrated that the chemical variations in britholite and apatite are related by the coupled substitution:

$$REE^{3+} + Si^{4+} = Ca^{2+} + P^{5+} \quad (1)$$

Figure 7A illustrates this substitution scheme with data from the Rodeo de los Molles deposit. Note that the strong negative correlation between Si + REE and Ca + P holds for all samples, irrespective of the alteration state and setting of the fluorbritholite-(Ce) and fluorapatite phases. According to this plot, the maximum proportion of fluorbritholite-(Ce) components in fluorapatite is ~14 %. Figure 7 further reveals a compositional gap of ~4 apfu between fluorbritholite-(Ce) and fluorapatite minerals at Rodeo de los Molles. Compositional gaps were also noted by Melluso et al. (2012), Macdonald et al. (2013), and Zozulya et al. (2017), suggesting the presence of a miscibility gap between the two mineral groups. The dashed grey line on figure 7A represents the balanced exchange of only those elements listed on the x- and y-axes. It is noted that there is a clear difference between the unaltered and altered fluorbritholite-(Ce) on this plot. All data from altered fluorbritholite-(Ce) plot below the dashed line, implying that additional components and more complex substitution schemes are involved. Other well-known substitution schemes are $Na^{+} + REE^{3+} = 2Ca^{2+}$ (Roeder et al. 1987; Rønsbo 1989) and $Th^{4+} + Si^{4+} = Ca^{2+} + 2P^{5+}$ (Pan and Fleet 2002; Pekov et al. 2011). These are insignificant in our case because Na is below the detection limit and the Th/U atomic ratios show no clear correlation between each other. Instead, our geochemical data point to the role of CO_3^{2-} as an additional substitution factor. As noted above, the excess F contents in fluorbritholite-(Ce) and fluorapatite suggest the presence of carbonate during crystallization of these phases (Piccoli and Candela 2002). The presence of Raman CO_3^{2-}

bands in fluorbritholite-(Ce) replacement structures (Fig. 5; rare-earth fluorcarbonates replacing fluorbritholite-(Ce)) further indicates the strong influence of carbonate during alteration of fluorbritholite-(Ce). This is also supported by H_2O-CO_2 fluid inclusions in fluorite crystals associated with the formation of bastnaesite (a rare-earth fluorcarbonate; Lira and Ripley 1990). The decrease in F contents of altered fluorbritholite-(Ce) indicates the replacement of c-axis anions by CO_3^{2-} as the controlling mechanism for the incorporation of carbonate ions into the britholite structure (Pan and Fleet 2002).

Implications of intergrowth textures as exsolution and miscibility gap

Micron-scale intergrowth textures between fluorbritholite-(Ce) and fluorapatite shown in Figure 3 (and Supplementary Fig. 1 and 2) have not been described so far in other britholite occurrences. These textures bear resemblance to symplectites, which commonly form at grain boundaries by mineral-fluid reaction. However, we rule out a reaction origin because (i) the inclusion blebs are randomly distributed in the host grains, but not near the grain boundaries (Fig. 3 C+D, Supplementary Fig. 1); (ii) type 1 intergrowths occur in fluorbritholite-(Ce) completely enclosed by zircon and titanite and thus removed from external fluids; (iii) the optical continuity of the host crystals (Fig. 3 A+B, Supplementary Fig. 1) is contrary to observations in symplectites, where several centers of growth are typical (Wall et al. 1993); and (iv) fluorbritholite-(Ce) and fluorapatite mutually include each other in type 1 and type 2 intergrowths, which is consistent with unmixing but difficult to explain by a reaction process. An alternative explanation for the intergrowth textures could be the crystallization of two phases on a cotectic, as in the graphic intergrowth of alkali-feldspar and quartz in granites and granophyres (Vernon 2004; Wall et al. 1993). However, there is no information on the phase relations of britholite-group minerals to test this, but we note that the growth of cotectic phases generally shows a crystallographic orientation, whereas most of the fluorapatite-fluorbritholite-(Ce) intergrowths have semi- or non-coherent interfaces. Unfortunately, direct

analysis of both intergrowth pairs was impossible because of their small size, but X-ray element maps (Supplementary Fig. 2) support the exchange relation shown in equation 1. Therefore, we suggest that the intergrowths are exsolution textures, which is consistent with the inferred miscibility gap between the two phases (Fig. 7A). However, a solvus has not yet been experimentally verified in this mineral group, but other studies of late-magmatic britholite also reported compositional gaps (Melluso et al. 2012; Macdonald et al. 2013; Zozulya et al. 2017). Though none of these gave robust temperature estimates, a general correlation between lower crystallization temperatures and larger compositional gaps, as implied by a solvus, can be drawn. The study of Melluso et al. (2012) of trachyphonolotic lava domes represents a volcanic setting and they reported the smallest compositional gap (< 1 apfu) between apatite und britholite. Zozulya et al. (2017) and Macdonald et al. (2013) found wider compositional gaps (~ 1.25 apfu and ~ 3 apfu, respectively) in samples from late-stage REE mineralization in pegmatites and granites. The Rodeo de los Molles mineralization is clearly post-magmatic hydrothermal, and a lower temperature of crystallization than the other studies is inferred (Fig. 7B). Thus, qualitatively, the evidence suggests a compositional gap between fluorapatite and fluorbritholite-(Ce), which increases with cooling (Fig. 7B) and matches the trend of a proposed solvus.

Post crystallization alteration

Gay and Lira (1984) were the first to observe the metamict transformation of britholite group minerals at Rodeo de los Molles as well as their later replacement by bastnaesite. They describe a partial replacement with one-half of some prismatic grains metamictized whereas the other bastnaesite half represents the carbonation front. In this study, the low oxide totals (86-97 wt.%) of the altered fluorbritholite-(Ce) grains, their high porosity, Raman spectral evidence for CO_3^{2-} groups, as well as the resorption and cracking textures are further indicators for hydration/carbonation of fluorbritholite-(Ce) at Rodeo de los Molles. The

polygonal cracks in strong alteration zones (Fig. 8) show strong similarities with the "mosaic textures" of $ThSiO_4$ phases described by Seydoux-Guillaume et al. (2007) and Macdonald et al. (2015). Those authors relate these textures to the formation of a gel-like amorphous, highly porous, and probably hydrated substance, initially caused by radiation damage. Natural radiation damage by alpha-decay events of U and Th has been variably described by "metamictization" and "amorphization". Irradiation often initiates lattice destruction at grain boundaries. This becomes visible under the microscope, where the studied fluorbritholite-(Ce) shows a darker grey-brownish color and the birefringence approaches zero (sensibly isotropic). Generally, silicates such as britholite are more susceptible to alpha decay-induced amorphization than phosphates like apatites (Weber et al. 1998). This might explain why fluorapatites, that are intergrown with altered fluorbritholite-(Ce), show no signs of alteration (e.g. lack of porosity) at Rodeo de los Molles. The radiation-damaged lattice structure ultimately facilitates alteration by fluids.

Implications

In this study of coexisting fluorbritholite-(Ce), britholite-(Ce) and fluorapatite, we presented EMP analyses of the minerals that demonstrate a range of fluorapatite and fluorbritholite-(Ce) compositions conforming to the substitution mechanism REE + Si = Ca + P. Moreover, the data demonstrate a compositional gap, which has been proposed before. What is new in this study, however, is the discovery of exsolution textures, which make it very likely that a miscibility gap between fluorapatite and fluorbritholite-(Ce) does exist, which suggests a potential experimental study on the miscibility between the two phases.

In general, fluorbritholite-(Ce) grains from Rodeo de los Molles are strongly altered and many features of the altered phases indicate that the mineral was affected by radiation damage caused by its high ThO_2 (2.19 wt.%) and UO_2 (1.32 wt.%) concentrations. Further studies of britholite metamictization and its influence on alteration processes (hydration,

carbonation, volume increase) could be of particular importance for the field of nuclear waste containment, since phases with the britholite structure have been used to store liquid nuclear waste (Livshits 2006).

Acknowledgements

We are grateful to Nicolas Viñas from Michelloti e Hijos, Córdoba, for accompanying us in the field and helping with drill core samples. We thank our reviewers Ray Macdonald and Kathy Ehrig as well as the associated Editor Dan Harlov for their comments and suggestions, which helped to improve this manuscript. The study is implemented in the framework of the international research training group StRATEGy (Surface Processes, Tectonics and Georesources: The Andean foreland basin of Argentina, IGK-2018) and was done in cooperation with the CONICET in Argentina. Our research was funded by the Deutsche Forschungsgemeinschaft (DFG, grant STR 373/34-1) and the Brandenburg Ministry of Sciences, Research and Cultural Affairs, Germany.

References

Ahijado, A., Casillas, R., Nagy, G., and Fernández, C. (2005) Sr-rich minerals in a carbonatite skarn, Fuerteventura, Canary Islands (Spain). Mineralogy and Petrology, 84(1-2), 107-127.

Arden, K.M., and Halden, N.M. (1999) Crystallization and alteration history of britholite in rare-earth-element-enriched pegmatitic segregations associated with the Eden Lake Complex, Manitoba, Canada. The Canadian Mineralogist, 37(5), 1239-1253.

Barrat, J. A., Zanda, B., Moynier, F., Bollinger, C., Liorzou, C., and Bayon, G. (2012) Geochemistry of CI chondrites: Major and trace elements, and Cu and Zn isotopes. Geochimica et Cosmochimica Acta, 83, 79-92.

Brugger, J., Ogierman, J., Pring, A., Waldron, H., and Kolitsch, U. (2006) Origin of the secondary REE-minerals at the Paratoo copper deposit near Yunta, South Australia. Mineralogical Magazine, 70(6), 609-627.

Carroll, J.D., and Chang, J.-J. (1970) Analysis of individual differences in multidimensional scaling via an n-way generalization of "Eckart-Young" decomposition. Psychometrika 35, 283–319.

Della Ventura, G., Williams, C.T., Cabella, R., Oberti, R., Caprilli, E., and Bellatreccia, F. (1999) Britholite-hellandite intergrowths and associated REE-minerals from the alkali-syenitic ejecta of the Vico volcanic complex (Latium, Italy); petrological implications bearing on REE mobility in volcanic systems. European Journal of Mineralogy, 11(5), 843-854.

Ferguson, M., Kamenetsky, V., Agangi, A., Kamenetsky, M., Meffre, S., and Ehrig, K. (2016) Iron and REE-bearing mineral assemblages in the rocks hosting the Olympic Dam and Wirrda Well IOCG deposits. Australian Earth Sciences Convention, 1.

Frost, R.L., and Dickfos, M.J. (2007). Raman spectroscopy of halogen-containing carbonates. Journal of Raman Spectroscopy 38(11), 1516-1522.

Gay, H.D., and Lira, R. (1984) Mineralización torífera y de tierras raras en el extremo septentrional del batolito de Las Chacras, San Luis. IX Congreso Geológico Argentino, 7, 342-356.

Gu, J., Chao, G.Y., and Tang, S. (1994) A new mineral–fluorbritholite-(Ce). Journal of Wuhan University Technology, 9(3), 9-14.

Harshman, R.A. (1970). PARAFAC. UCLA Working Papers in Phonetics 16, 1–84.

Holtstam, D., and Andersson, U.B. (2007) The REE minerals of the Bastnas-type deposits, south-central Sweden. The Canadian Mineralogist, 45(5), 1073-1114.

Lafuente, B., Downs, R.T., Yang, H., Stone, N., Armbruster, T., and Danisi, R.M. (2015) Highlights in mineralogical crystallography. W. De Gruyter, Berlin, 1-30.

Lira, R., and Ripley, E.M. (1990) Fluid inclusion studies of the Rodeo de Los Molles REE and Th deposit, Las Chacras Batholith, Central Argentina. Geochimica et Cosmochimica Acta, 54, 663-671.

Lira, R., and Ripley, E.M. (1991) Reply to comment on "Fluid inclusion studies of the Rodeo de Los Molles REE and Th deposit, Las Chacras Batholith, Central Argentina". Geochimica et Cosmochimica Acta, 55,2065-2066.

Lira, R., and Ripley, E.M. (1992) Hydrothermal alteration and REE-Th mineralization at the Rodeo de Los Molles deposit, Las Chacras batholith, central Argentina. Contributions to Mineralogy and Petrology, 110(2-3), 370-386.

Lira, R., Viñas, N.A., Ripley, E.M., and Barbieri, M. (1999) El yacimiento de tierras raras, torio y uranio Rodeo de los Molles, San Luis. Recursos Minerales de la República Argentina: Instituto de Geología y Recursos Minerales, Servicio Geológico Minero Argentino, Anales, 35, 987-997.

Livshits, T.S. (2006) Britholites as natural analogues of actinide matrices: Resistance to radiation damage. Geology of Ore Deposits, 48(5), 357-368.

López de Luchi, M.G.L., Siegesmund, S., Wemmer, K., and Nolte, N. (2017) Petrogenesis of the postcollisional Middle Devonian monzonitic to granitic magmatism of the Sierra de San Luis, Argentina. Lithos, 288, 191-213.

Macdonald, R., Bagiński, B., Dzierżanowski, P., and Jokubauskas, P. (2013) Apatite-supergroup minerals in UK Palaeogene granites: composition and relationship to host-rock composition. European Journal of Mineralogy, 25(3), 461-471.

Macdonald, R., Bagiński, B., Kartashov, P.M., Zozulya, D., Dzierżanowski, P., and Jokubauskas, P. (2015) Hydrothermal alteration of a chevkinite-group mineral to a bastnäsite-(Ce)-ilmenite-columbite-(Fe) assemblage: interaction with a F-, CO_2-rich fluid. Mineralogy and Petrology, 109(6), 659-678.

Melluso, L., De'Gennaro, R., Fedele, L., Franciosi, L., and Morra, V. (2012) Evidence of crystallization in residual, Cl–F-rich, agpaitic, trachyphonolitic magmas and primitive Mg-rich basalt–trachyphonolite interaction in the lava domes of the Phlegrean Fields (Italy). Geological Magazine, 149(3), 532-550.

Melluso, L., Guarino, V., Lustrino, M., Morra, V., and De'Gennaro, R. (2017) The REE-and HFSE-bearing phases in the Itatiaia alkaline complex (Brazil) and geochemical evolution of feldspar-rich felsic melts. Mineralogical Magazine, 81(2), 217-250.

Nash, W.P. (1972) Apatite chemistry and phosphorus fugacity in a differentiated igneous intrusion. American Mineralogist, 57(5-6), 877-886.

Oberti, R., Ottolini, L., Ventura, G.D., and Parodi, G.C. (2001) On the symmetry and crystal chemistry of britholite: New structural and microanalytical data. American Mineralogist, 86(9), 1066-1075.

Orlandi, P., Perchiazzi, N., and Mannucci, G. (1989) First occurrence of britholite-(Ce) in Italy (Monte Somma, Vesuvius). European Journal of Mineralogy, 723-725.

Ouzegane, K., Fourcade, S., Kienast, J.R., and Javoy, M. (1988) New carbonatite complexes in the Archaean In'Ouzzal nucleus (Ahaggar, Algeria): mineralogical and geochemical data. Contributions to Mineralogy and Petrology, 98(3), 277-292.

Pan, Y., and Fleet, M.E. (2002) Compositions of the apatite-group minerals: substitution mechanisms and controlling factors. Reviews in Mineralogy and Geochemistry, 48(1), 13-49.

Pasero, M., Kampf, A.R., Ferraris, C., Pekov, I.V., Rakovan, J., and White, T.J. (2010) Nomenclature of the apatite supergroup minerals. European Journal of Mineralogy, 22(2), 163-179.

Pekov, I.V., Zubkova, N.V., Chukanov, N.V., Husdal, T.A., Zadov, A.E., and Pushcharovsky, D.Y. (2011) Fluorbritholite-(Y),(Y, Ca, Ln) 5 [(Si, P) O4] 3 F, a new mineral of the

britholite group. Neues Jahrbuch für Mineralogie-Abhandlungen: Journal of Mineralogy and Geochemistry, 188(2), 191-197.

Piccoli, P.M., and Candela, P.A. (2002) Apatite in igneous systems. Reviews in Mineralogy and Geochemistry, 48(1), 255-292.

Rakovan, J.F., and Hughes, J.M. (2000) Strontium in the apatite structure: strontian fluorapatite and belovite-(Ce). The Canadian Mineralogist, 38(4), 839-845.

Roeder, P.L., MacArthur, D., Ma, X.P., Palmer, G.R., and Mariano, A.N. (1987) Cathodoluminescence and microprobe study of rare-earth elements in apatite. American Mineralogist, 72(7-8), 801-811.

Rønsbo, J.G. (1989) Coupled substitutions involving REEs and Na and Si in apatites in alkaline rocks from the Ilimaussaq intrusion, South Greenland, and the petrological implications. American Mineralogist, 74(7-8), 896-901.

Seydoux-Guillaume, A.M., Wirth, R., and Ingrin, J. (2007) Contrasting response of $ThSiO_4$ and monazite to natural irradiation. European Journal of Mineralogy, 19(1), 7-14.

Siegesmund, S., Steenken, A., López de Luchi, M.G., Wemmer, K., Hoffmann, A., and Mosch, S. (2004) The Las Chacras-Potrerillos batholith (Pampean Ranges, Argentina): structural evidences, emplacement and timing of the intrusion. International Journal of Earth Sciences, 93(1), 23-43.

Torró, L., Villanova, C., Castillo, M., Campeny, M., Melgarejo, J.C., and Gonçalves, A.O. (2012) Niobium and rare earth minerals from the Virulundo carbonatite, Namibe, Angola. Mineralogical Magazine, 76(2), 393-409.

Uher, P., Ondrejka, M., Bačík, P., Broska, I., and Konečný, P. (2015) Britholite, monazite, REE carbonates, and calcite: Products of hydrothermal alteration of allanite and apatite in A-type granite from Stupné, Western Carpathians, Slovakia. Lithos, 236, 212-225.

Vernon, R.H. (2004) A practical guide to Rock Microstructure. University Press, Cambridge, UK, 594 p.

Wall, F., Le Bas, J., and Srivastava, R.K. (1993) Calcite and carbocernaite exsolution and cotectic textures in a Sr, REE-rich carbonatite dyke from Rajasthan, India. Mineralogical Magazine, 57, 388, 495-513.

Weber, W.J., Ewing, R.C., Catlow, C.R.A., De La Rubia, T.D., Hobbs, L.W., Kinoshita, C., and Vance, E.R. (1998) Radiation effects in crystalline ceramics for the immobilization of high-level nuclear waste and plutonium. Journal of Materials Research, 13(6), 1434-1484.

Winther, C. (1901): Britholith, a new mineral. Meddelelser om Grønland, 24,190–196.

Zozulya, D.R., Lyalina, L.M., and Savchenko, Y.E. (2015) Britholite ores of the Sakharjok Zr–Y–REE deposit, Kola Peninsula: Geochemistry, mineralogy, and formation stages. Geochemistry International, 53(10), 892-902.

Zozulya, D.R., Lyalina, L.M., and Savchenko, Y.E. (2017) Britholite-group minerals as sensitive indicators of changing fluid composition during pegmatite formation: evidence from the Keivy alkaline province, Kola peninsula, NW Russia. Mineralogy and Petrology, 111(4), 511-522.

Figure captions:

Figure 1: A) Geological map of the Las-Chacras-Potrerillos batholith, modified after Siegesmund et al. (2004). B) Google Earth satellite image of the REE deposit Rodeo de los Molles. White dashed outline delineates the fenite zone (from Gay and Lira 1984), EG: equigranular granite, PG: porphyritic granite.

Figure 2: Illustration of the REE mineralization at Rodeo de los Molles: A) Outcrop photograph of a fluorbritholite-(Ce)-rich vein (FBri-vein; white outlined) in fenite, lens cap for scale. B) Photomicrograph in transmitted light of the contact between a fluorbritholite-(Ce)-rich vein and surrounding fenite (see drill core section in image D). A transition zone (TZ, black dashed outline) between the fenite and fluorbritholite-(Ce) vein is rich in albite. C) Photomicrograph in transmitted light showing a typical structure of a REE-rich composite (REE fluorcarbonates, fluorapatite, fluorite ± fluorbritholite-(Ce)) within the fenite. D) Drill core sample of the fluorbritholite-(Ce)-rich vein in A, at 22.5 m depth. This sample further contains late stage quartz (Qz), fluorite (Flr) and carbonate (Cb) veins cross-cutting the feldspar-rich (Fsp) fenite.

Figure 3: Backscattered EMP images of REE mineralization in fluorbritholite-(Ce) rich vein (A-F) and patchy REE-rich composites (E+F). A) Aggregate of hydrothermal zircon with straight grain boundaries (Zrn: white dashed outline) containing euhedral crystals of fluorbritholite-(Ce) (FBri-0) with irregular inclusions of fluorapatite (FAp-0). The surrounding phases are fluorbritholite-(Ce)-fluorapatite-aggregates (FBri, FAp), plagioclase (Pl), and quartz (Qz). B) Titanite aggregate (Ttn: white dashed outline) containing euhedral fluorbritholite-(Ce) crystals (FBri-0) with exsolution-like blebs of fluorapatite (FAp-0), surrounded by fluorbritholite-(Ce) (FBri), fluorapatite (FAp), quartz (Qz) and minor

plagioclase (Pl). C) A large fluorapatite grain (FAp) with patchy zoning (light and dark grey) and bleb-like fluorbritholite-(Ce) inclusions (FBri-0). The fluorapatite is surrounded by Fluorbritholite-(Ce) (FBri) and quartz (Qz). D) Intergrowths of fluorbritholite-(Ce) and fluorapatite with minor plagioclase (Pl) and K-feldspar (Kfsp). The central grain shows an exsolution-like lamellae and blebs of fluorapatite. E) Large euhedral fluorapatite grains (FAp-a) intergrown with allanite-(Ce) (Aln) and surrounded by hydrothermal quartz (Qz), at the edge of an REE-rich composite structure (REE fluorcarbonates, fluorapatite, fluorite ± fluorbritholite-(Ce)). F) Large fluorapatite (FAp-a) crystal intergrown with a REE-rich composite, and allanite-(Ce) (Aln) and surrounded by hydrothermal quartz (Qz). Note a younger generation of inclusion free fluorapatites (FAp-b) within the allanite-(Ce) areas (lower right of the image).

Figure 4: Electron microprobe analyses of fluorbritholite-(Ce) and fluorapatite minerals from Rodeo de los Molles plottet on a classification diagram of apatite-supergroup minerals (after Passero et al. 2010; Uher et al. 2015). The few points in the britholite field are from highly altered grains within the transition zone between the vein mineralization and the surrounding fenite (see Fig. 2B). INT 1 and INT2 on the legend, for intergrowth type 1 and 2, see text.

Figure 5: Raman spectra of an altered fluorbritholite-(Ce) grain in the vein mineralization, showing characteristic bands for rare-earth fluorcarbonates at 265, 601, 745 and 1096 cm^{-1} (Frost and Dickfos 2007; Lafuente et al. 2015). Typical CO_3^{2-} vibrational modes were assigned at 745 (CO_3^{2-} bending mode), 1096 cm^{-1} (CO_3^{2-} symmetric stretching mode), and between 1300-1500 cm^{-1} (CO_3^{2-} asymmetric stretching mode) according to Frost and Dickfos (2007).

Figure 6: Chondrite-normalized REE-concentrations of fluorbritholite-(Ce) and fluorapatite minerals (incomplete spectra) compared with bulk analysis of the fluorbritholite-(Ce) vein shown in Figure 2A. Britholite REE data from Arden and Halden (1999) and Macdonald et al. (2013) are shown for comparison. Normalization after Barrat et al. (2012).

Figure 7: A: Illustration of fluorbritholite-(Ce) and fluorapatite compositions from Rodeo de los Molles plotted in terms of the dominant cation substitution scheme between apatite- and britholite-group members: REE + Si (x-axis) vs. Ca + P (y-axis). The dashed line represents the exchange vector (Si + REE) = (Ca + P), which fits the analyses well. Points plotting of this line (mostly altered fluorbritholite-(Ce)) are affected by other substitutions. B: Illustration of the correlation between the size of the compositional gaps from this and other studies and the relative formation temperatures of the different britholite occurrences.

Figure 8: Illustrations of post-crystallization alteration features in REE minerals from Rodeo de los Molles. A) Backscattered electron image of a fluorbritholite-(Ce)-fluorapatite aggregate (in vein mineralization) showing desiccation or shrinkage cracks in fluorbritholite-(Ce) (FBri-2) The fluorbritholite-(Ce) grains (FBri) also show secondary dissolution-replacement textures (darker grey patches). The surrounding plagioclase (Pl) and alkali-feldspar (Kfsp) grains show cleavage-parallel fractures filled with REE and Mn-rich phases. B) Secondary electron image of a patchy REE carbonate composite with REE-rich secondary assemblages (fluorapatite + REE fluorcarbonate + fluorite ± fluorbritholite-(Ce)) surrounded by allanite-(Ce) (Aln) and an outer rim with euhedral, inclusion free fluorapatite grains (FAp-b) and quartz (upper right corner). The center of the REE composite shows intense cracking, presumably caused by volume change.

Supplementary Figure 1: Simplified sketches of intergrowth types 1 and 2, extracted from backscattered electron images of Figure 3. **A)** Type 1: a euhedral fluorbritholite-(Ce) grain enclosed by titanite (Fig. 3B) and containing variably-oriented vermicular fluorapatite, locally in a parallel arrangement. **B)** Type 1: a large fluorbritholite-(Ce) aggregate containing vermicular inclusions of fluorapatite in the central part and very small, parallel-oriented blebs of fluorapatite along grain boundaries (upper and left side of the image) within another fluorbritholite-(Ce) grain (see Fig. 3D). Note two orientations of fluorapatite inclusions in the central part, one parallel to the c-axis, the other at a high angle to it. **C)** Type 2: a fluorapatite host with parallel oriented vermicular inclusions of fluorbritholite-(Ce). **D)** Type 2: a large fluorapatite grain with variable sizes and arrangements of fluorbritholite-(Ce) inclusions (see Fig. 3C), which are locally parallel oriented (left side of image). Note the very fine-grained cross-cutting fractures that are filled with REE-rich phases.

Supplementary Figure 2: Backscattered electron image, simplified sketch and microprobe X-ray element maps of a single fluorbritholite-(Ce) grain included in hydrothermal zircon (Type 1 intergrowth, see Fig. 3A). The sketch emphasizes the arrangement and shapes of fluorapatite inclusions. The four lower images show element maps of Ca, P, Ce and Si in the fluorbritholite-(Ce) host and fluorapatite inclusions. Note the positive correlation between Ce + Si and Ca + P within both mineral phases, which supports the interpretation that these are exsolution textures (Fig. 7).

This is a preprint, the final version is subject to change, of the American Mineralogist (MSA)
Cite as Authors (Year) Title. American Mineralogist, in press.
DOI: https://doi.org/10.2138/am-2019-6969

Table 1. Representative compositions (wt.%) and structural formulae (apfu) of fluorbritholite-(Ce).

	Unaltered Fluorbritholites			**Altered Fluorbritholites**								
	FBri 1	**FBri 1**	**FBri 2**	**FBri 3**	**FBri 4**	**FBri 5**	**FBri 6**	**FBri 7**	**FBri 8**	**FBri 9**	**FBri 10**	**FBri 11**	**FBri 12**
P_2O_5	2.77	2.81	5.79	6.65	2.04	3.84	3.29	6.21	2.56	5.23	6.54	5.69	4.02
SiO_2	19.88	20.21	18.34	20.55	21.96	21.56	23.95	19.47	14.01	20.16	21.96	16.07	18.95
ThO_2	1.80	2.13	0.49	1.69	1.99	1.96	2.28	1.92	1.26	2.19	1.87	1.95	1.46
UO_2	0.71	0.80	0.51	0.66	0.57	0.68	0.59	1.32	0.41	1.06	0.68	0.69	0.52
Al_2O_3	b.d.l.	b.d.l.	b.d.l.	0.33	0.06	0.21	0.91	b.d.l.	b.d.l.	b.d.l.	b.d.l.	b.d.l.	0.13
Y_2O_3	1.77	1.94	1.81	1.91	1.75	1.95	1.90	2.17	2.89	2.17	2.32	2.14	1.19
La_2O_3	11.17	10.25	9.74	12.35	11.52	10.94	10.00	11.79	8.46	11.51	10.23	11.43	10.99
Ce_2O_3	27.04	26.66	24.45	23.54	24.84	24.09	23.62	28.47	25.49	25.85	25.81	28.90	24.90
Pr_2O_3	2.94	3.08	2.81	3.17	3.11	2.89	3.05	3.15	3.59	3.18	3.01	3.20	3.07
Nd_2O_3	10.95	11.55	10.47	11.73	11.58	11.16	11.01	12.01	14.31	12.09	11.78	12.00	11.36
Sm_2O_3	1.22	1.35	1.10	1.08	1.16	1.09	1.14	1.29	1.70	1.32	1.32	1.21	1.07
Eu_2O_3	0.18	0.19	0.18	0.17	0.19	0.19	0.19	0.19	0.24	0.20	0.20	0.23	0.19
Gd_2O_3	1.53	1.60	1.72	1.79	1.84	1.81	1.79	1.74	1.97	1.51	1.91	1.99	1.87
Tb_2O_3	b.d.l.	b.d.l.	b.d.l.	b.d.l.	0.15	b.d.l.	b.d.l.	b.d.l.	b.d.l.	b.d.l.	b.d.l.	b.d.l.	b.d.l.
Dy_2O_3	0.40	0.37	0.33	0.31	0.39	0.36	0.40	0.37	0.54	0.35	0.45	0.36	0.36
Er_2O_3	b.d.l.	b.d.l.	b.d.l.	b.d.l.	b.d.l.	0.15	0.15	0.16	b.d.l.	0.17	0.17	0.17	0.17
Yb_2O_3	b.d.l.	b.d.l.	b.d.l.	b.d.l.	b.d.l.	0.11	b.d.l.	b.d.l.	b.d.l.	b.d.l.	0.17	0.14	0.13
CaO	13.79	14.01	16.80	5.89	6.92	7.20	5.48	3.96	10.61	5.42	2.78	2.91	3.79
MnO	0.35	0.34	0.35	b.d.l.	b.d.l.	0.64	0.00	0.54	0.63	0.37	0.55	0.53	b.d.l.
FeO	b.d.l.	b.d.l.	b.d.l.	b.d.l.	b.d.l.	b.d.l.	b.d.l.	b.d.l.	b.d.l.	b.d.l.	0.15	b.d.l.	b.d.l.
SrO	b.d.l.	b.d.l.	b.d.l.	b.d.l.	b.d.l.	b.d.l.	b.d.l.	b.d.l.	b.d.l.	b.d.l.	b.d.l.	b.d.l.	b.d.l.
PbO	0.09	0.14	0.04	0.14	0.17	0.23	0.18	0.21	0.07	0.13	0.06	0.20	0.13
Na_2O	b.d.l.	b.d.l.	b.d.l.	b.d.l.	b.d.l.	b.d.l.	b.d.l.	b.d.l.	b.d.l.	b.d.l.	b.d.l.	b.d.l.	0.02
H_2O_{calc}	-	0.10	0.02	0.10	-	-	0.32	0.42	-	0.07	0.39	0.59	0.49
SO_3	b.d.l.	b.d.l.	b.d.l.	b.d.l.	b.d.l.	b.d.l.	b.d.l.	b.d.l.	b.d.l.	b.d.l.	b.d.l.	b.d.l.	b.d.l.
F	2.64	2.17	2.50	2.16	2.53	2.47	1.66	1.42	2.67	2.16	1.54	0.82	1.00

This is a preprint, the final version is subject to change, of the American Mineralogist (MSA)
Cite as Authors (Year) Title. American Mineralogist, in press.
DOI: https://doi.org/10.2138/am-2019-6969

Sum	99.59	100.15	97.88	94.73	92.98	91.08	92.22	97.28	91.82	95.43	94.05	91.47	86.02
Formulae on the basis of 13 oxygens													
P	0.299	0.315	0.607	0.748	0.233	0.425	0.378	0.720	0.321	0.606	0.743	0.740	0.528
Si	2.533	2.676	2.272	2.730	2.965	2.821	3.246	2.668	2.074	2.761	2.948	2.469	2.940
S	0.000	0.000	0.000	0.000	0.000	0.000	0.000	0.000	0.000	0.000	0.000	0.000	0.000
Sum T	2.833	2.992	2.882	3.481	3.198	3.249	3.624	3.398	2.400	3.371	3.695	3.213	3.476
Th	0.052	0.064	0.014	0.051	0.061	0.058	0.070	0.060	0.042	0.068	0.057	0.068	0.052
U	0.020	0.024	0.014	0.020	0.017	0.020	0.018	0.040	0.013	0.032	0.020	0.024	0.018
Al	0.000	0.000	0.000	0.052	0.010	0.033	0.146	0.000	0.000	0.000	0.000	0.000	0.023
Y	0.120	0.137	0.119	0.135	0.126	0.136	0.137	0.158	0.228	0.158	0.166	0.175	0.098
La	0.525	0.500	0.445	0.605	0.574	0.528	0.500	0.596	0.462	0.581	0.506	0.648	0.629
Ce	1.261	1.292	1.109	1.145	1.228	1.154	1.172	1.428	1.381	1.296	1.268	1.625	1.414
Pr	0.136	0.149	0.127	0.153	0.153	0.138	0.151	0.157	0.194	0.159	0.147	0.179	0.173
Nd	0.498	0.546	0.463	0.556	0.558	0.521	0.533	0.588	0.756	0.591	0.565	0.658	0.629
Sm	0.054	0.062	0.047	0.049	0.054	0.049	0.053	0.061	0.087	0.062	0.061	0.064	0.057
Eu	0.008	0.008	0.008	0.008	0.009	0.008	0.009	0.009	0.012	0.009	0.009	0.012	0.010
Gd	0.065	0.070	0.070	0.079	0.082	0.078	0.080	0.079	0.097	0.069	0.085	0.101	0.096
Tb	0.000	0.000	0.000	0.000	0.000	0.000	0.000	0.000	0.000	0.000	0.000	0.000	0.000
Dy	0.016	0.016	0.013	0.013	0.017	0.015	0.017	0.016	0.026	0.015	0.020	0.018	0.018
Er	0.000	0.000	0.000	0.000	0.000	0.010	0.010	0.007	0.000	0.007	0.007	0.008	0.010
Yb	0.000	0.000	0.000	0.000	0.000	0.004	0.000	0.000	0.000	0.000	0.007	0.006	0.010
Ca	1.882	1.987	2.230	0.838	1.001	1.009	0.796	0.581	1.683	0.795	0.400	0.479	0.630
Mn	0.038	0.039	0.037	0.000	0.000	0.071	0.000	0.063	0.079	0.043	0.063	0.069	0.000
Fe	0.001	0.000	0.000	0.000	0.001	0.002	0.003	0.004	0.006	0.002	0.017	0.004	0.000
Sr	0.000	0.000	0.000	0.000	0.000	0.000	0.000	0.000	0.000	0.000	0.000	0.000	0.000
Pb	0.006	0.010	0.003	0.014	0.016	0.021	0.017	0.020	0.006	0.012	0.006	0.019	0.014
Na	0.000	0.000	0.000	0.000	0.000	0.000	0.000	0.000	0.000	0.000	0.000	0.000	0.005
Sum M	4.700	4.921	4.715	3.737	3.925	3.859	3.720	3.882	5.097	3.912	3.410	4.168	3.887
F	1.065	0.910	0.979	0.908	1.078	1.021	0.713	0.614	1.250	0.934	0.655	0.398	0.488
OH_{calc}	-	0.090	0.021	0.092	-	-	0.287	0.386	-	0.066	0.345	0.602	0.512
Sum X	1.000	1.000	1.000	1.000	1.000	1.000	1.000	1.000	1.000	1.000	1.000	1.000	1.000

b.d.l. – below detection limit.

This is a preprint, the final version is subject to change, of the American Mineralogist (MSA)
Cite as Authors (Year) Title. American Mineralogist, in press.
DOI: https://doi.org/10.2138/am-2019-6969

FBri1: Unaltered atoll fluorbritholite-(Ce) of the vein mineralization. F*Bri2:* Relatively unaltered atoll fluorbritholite-(Ce) within the transition zone (TZ). F*Bri3:* Exsolved fluorbritholite-(Ce) (FBri-0, e.g. Fig. 3C) within a fluorapatite grain (FAp), showing alteration with porosity. F*Bri4:* Altered fluorbritholite-(Ce) grain with exsolution of fluorapatite and quartz (FBri-0 in Fig. 3D). F*Bri5:* Euhedral slightly altered fluorbritholite-(Ce) with exsolution textures of fluorapatite within a big titanite aggregate (FBri-0 in Fig. 3B). F*Bri6:* Euhedral altered fluorbritholite-(Ce) with exsolution like textures of fluorapatite within a big hydrothermal zircon aggregate (FBri-0 in Fig. 3A). F*Bri7:* Small unaltered euhedral britholite grain, inclusion and exsolution free, surrounded by newly formed allanite. F*Bri8:* Relatively unaltered relict of britholite in the center of a REE-rich composite. F*Bri9:* Alteration zone of a big fluorbritholite-(Ce) aggregate. F*Bri10:* Alteration zone of a fluorbritholite-(Ce) aggregate within the TZ. F*Bri11:* Altered fluorbritholite-(Ce) grain with sub-prismatic fractures, surrounded by allanite (TZ). F*Bri12:* Altered fluorbritholite-(Ce) grain with sub-prismatic fractures, showing high porosity.

This is a preprint, the final version is subject to change, of the American Mineralogist (MSA)
Cite as Authors (Year) Title. American Mineralogist, in press.
DOI: https://doi.org/10.2138/am-2019-6969

Table 2. Representative compositions (wt.%) and structural formulae (apfu) of fluorapatites.

	In vein mineralization								In REE-rich composite			
	FAp 1	**FAp 2**	**FAp 3**	**FAp 4**	**FAp 5**	**FAp 6**	**FAp 7**	**FAp 8**	**FAp 9**	**FAp 10**	**FAp 11**	**FAp 12**
P_2O_5	37.06	33.62	38.66	35.55	35.34	36.34	36.61	36.40	32.47	35.07	32.99	37.20
SiO_2	2.28	3.66	1.06	2.74	2.42	2.15	2.15	1.63	1.73	0.97	2.30	1.14
ThO_2	0.05	0.13	b.d.l.	0.18	0.05	0.06	0.06	0.03	0.07	0.06	b.d.l.	b.d.l.
UO_2	0.03	0.07	0.01	0.07	b.d.l.	0.02	0.02	0.01	0.05	0.02	0.06	b.d.l.
Al_2O_3	b.d.l.	b.d.l.	b.d.l.	b.d.l.	b.d.l.	b.d.l.	b.d.l.	b.d.l.	b.d.l.	b.d.l.	b.d.l.	b.d.l.
Y_2O_3	0.29	0.49	0.14	0.29	0.31	0.28	0.30	0.21	0.29	0.00	0.49	0.35
La_2O_3	1.14	1.86	0.56	1.65	1.30	1.21	1.16	0.97	0.85	0.35	0.70	0.41
Ce_2O_3	3.14	5.11	1.57	4.33	3.39	3.14	2.94	2.07	2.27	1.05	2.34	1.44
Pr_2O_3	0.40	0.58	0.17	0.41	0.40	0.38	0.37	0.27	0.35	0.20	0.44	0.17
Nd_2O_3	1.35	2.15	0.75	1.64	1.58	1.50	1.49	1.20	1.37	0.78	1.93	1.03
Sm_2O_3	0.17	0.27	0.08	0.22	0.18	0.15	0.20	0.11	b.d.l.	b.d.l.	0.26	b.d.l.
Eu_2O_3	0.03	0.03	b.d.l.	b.d.l.	0.03	b.d.l.	b.d.l.	b.d.l.	0.03	b.d.l.	0.04	b.d.l.
Gd_2O_3	0.22	0.32	0.12	0.29	0.23	0.24	0.21	0.16	0.18	0.13	0.27	b.d.l.
Tb_2O_3	b.d.l.	b.d.l.	b.d.l.	b.d.l.	b.d.l.	b.d.l.	b.d.l.	0.32	b.d.l.	b.d.l.	b.d.l.	b.d.l.
Dy_2O_3	b.d.l.	b.d.l.	b.d.l.	b.d.l.	b.d.l.	b.d.l.	b.d.l.	b.d.l.	b.d.l.	b.d.l.	b.d.l.	b.d.l.
Er_2O_3	b.d.l.	b.d.l.	b.d.l.	b.d.l.	b.d.l.	b.d.l.	b.d.l.	b.d.l.	b.d.l.	b.d.l.	b.d.l.	b.d.l.
Yb_2O_3	b.d.l.	b.d.l.	b.d.l.	b.d.l.	0.19	0.18	0.14	b.d.l.	b.d.l.	b.d.l.	b.d.l.	b.d.l.
CaO	49.35	46.53	51.87	47.89	48.97	49.09	49.43	50.63	49.79	52.22	48.70	51.42
MnO	0.06	0.11	b.d.l.	b.d.l.	0.08	0.06	0.08	b.d.l.	0.16	0.09	0.16	0.11
FeO	b.d.l.	b.d.l.	0.01	0.01	0.01	b.d.l.	0.02	b.d.l.	0.02	0.03	0.01	0.02
SrO	0.42	0.36	0.49	0.37	0.42	0.93	0.40	0.45	1.13	0.91	0.89	0.94
PbO	b.d.l.	0.02	b.d.l.	0.01	0.06	0.18	b.d.l.	0.01	0.03	0.02	0.10	0.39
Na_2O	0.24	0.21	0.13	0.14	0.38	0.20	0.27	0.12	0.26	0.12	0.23	0.11
H_2O_{calc}	0.43	0.40	0.18	0.32	0.41	0.32	0.42	0.12	0.39	0.37	0.29	0.42
SO_3	0.42	0.65	0.23	0.24	1.03	0.65	0.69	0.31	0.44	0.27	0.46	0.27
F	2.63	2.57	3.21	2.80	2.64	2.86	2.63	3.24	2.45	2.62	2.72	2.63
Sum	99.87	99.33	99.41	99.46	99.66	100.35	99.78	98.41	94.50	95.85	95.63	98.39

Formulae on the basis of 13 oxygens

P	2.806	2.632	2.885	2.745	2.701	2.763	2.780	2.787	2.654	2.770	2.656	2.841
Si	0.204	0.339	0.093	0.250	0.219	0.193	0.193	0.147	0.167	0.091	0.219	0.102
S	0.028	0.045	0.015	0.016	0.070	0.044	0.046	0.021	0.032	0.019	0.033	0.018
Sum T	3.038	3.016	2.993	3.011	2.990	3.000	3.019	2.955	2.853	2.879	2.908	2.962
Th	0.001	0.003	0.000	0.004	0.001	0.001	0.001	0.001	0.001	0.001	0.000	0.000
U	0.001	0.001	0.000	0.001	0.000	0.000	0.000	0.000	0.001	0.000	0.001	0.000
Al	0.000	0.000	0.000	0.005	0.000	0.000	0.000	0.000	0.000	0.000	0.000	0.000
Y	0.014	0.024	0.007	0.014	0.015	0.014	0.014	0.010	0.015	0.000	0.025	0.017
La	0.038	0.063	0.018	0.055	0.043	0.040	0.038	0.032	0.030	0.012	0.024	0.014
Ce	0.103	0.173	0.051	0.145	0.112	0.103	0.097	0.069	0.080	0.036	0.081	0.048
Pr	0.013	0.020	0.005	0.014	0.013	0.012	0.012	0.009	0.012	0.007	0.015	0.005
Nd	0.043	0.071	0.024	0.053	0.051	0.048	0.048	0.039	0.047	0.026	0.066	0.033
Sm	0.005	0.009	0.002	0.007	0.006	0.005	0.006	0.004	0.000	0.000	0.008	0.000
Eu	0.001	0.001	0.000	0.001	0.001	0.001	0.001	0.001	0.001	0.001	0.001	0.000
Gd	0.006	0.010	0.003	0.009	0.007	0.007	0.006	0.005	0.006	0.004	0.008	0.001
Tb	0.001	0.001	0.003	0.003	0.006	0.003	0.003	0.009	0.002	0.001	0.001	0.001
Dy	0.002	0.002	0.002	0.003	0.000	0.005	0.000	0.001	0.001	0.001	0.003	0.004
Er	0.001	0.001	0.000	0.001	0.000	0.000	0.001	0.001	0.001	0.001	0.002	0.001
Yb	0.000	0.001	0.000	0.001	0.005	0.005	0.004	0.000	0.000	0.001	0.000	0.001
Ca	4.729	4.611	4.898	4.679	4.737	4.723	4.751	4.905	5.150	5.219	4.962	4.970
Mn	0.004	0.009	0.000	0.000	0.006	0.005	0.006	0.000	0.013	0.007	0.013	0.008
Fe	0.000	0.000	0.001	0.000	0.001	0.000	0.002	0.000	0.002	0.002	0.001	0.001
Sr	0.022	0.019	0.025	0.020	0.022	0.049	0.021	0.023	0.063	0.049	0.049	0.049
Pb	0.000	0.001	0.000	0.001	0.003	0.009	0.000	0.001	0.001	0.001	0.005	0.018
Na	0.042	0.037	0.023	0.024	0.066	0.034	0.046	0.022	0.048	0.021	0.043	0.018
Sum M	5.027	5.058	5.062	5.039	5.097	5.067	5.058	5.132	5.478	5.403	5.312	5.193
F	0.743	0.753	0.895	0.807	0.754	0.811	0.746	0.926	0.748	0.773	0.818	0.750
OH_{calc}	0.257	0.247	0.105	0.193	0.246	0.189	0.254	0.074	0.252	0.227	0.182	0.250
Sum X	1.000	1.000	1.000	1.000	1.000	1.000	1.000	1.000	1.000	1.000	1.000	1.000

b.d.l. – below detection limit.

FAp1: Dark colored (BSE) grain of the vein mineralization (FAp in Fig. 3C). F*Ap2*: Light colored (BSE) part of the FAp1 grain. F*Ap3*: Fluorapatite grain with inclusions of fluorbritholite-(Ce) (intergrowth type 2). F*Ap4*: Fluorapatite exsolving in fluorbritholite-(Ce) (intergrowth type 1). F*Ap5*: Fluorapatite intergrown with fluorbritholite-(Ce) in the vein mineralization. F*Ap6*: Fluorapatite inclusion in a REE-rich composite close to the big fluorbritholite-(Ce) rich vein (Fig. 2A). F*Ap7*: Fluorapatite intergrown with fluorbritholite-(Ce) within the transition zone (TZ) (Fig. 2B). F*Ap8*: Inclusion of fluorapatite within an euhedral fluorbritholite-(Ce) crystal of intergrowth type 1 (Fig. 3A). F*Ap9*: Huge subhedral fluorapatite grain, light colored (BSE), intergrown with a REE-rich composite (FAp-a in Fig. 3E). F*Ap10*: Same grain, dark colored (BSE) part. F*Ap11*: Fluorpatite grain within a REE composite (Fig. 3F). F*Ap12*: Euhedral fluorapatite within allanite-(Ce) rim of a REE composite (FAp-b in Fig. 3F).

Fig 1

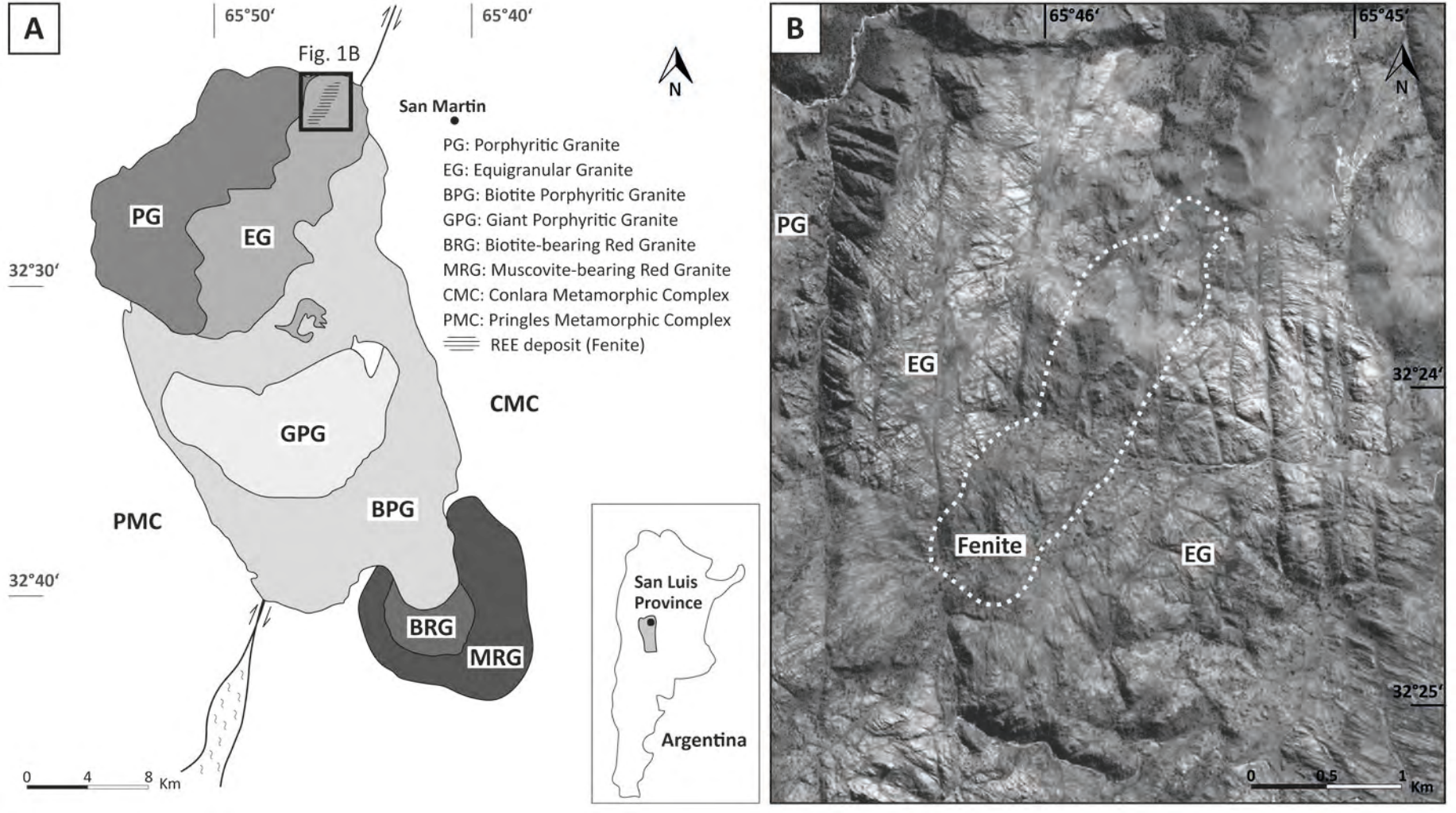
A
65°50′
65°40′
Fig. 1B
N
San Martin
PG: Porphyritic Granite
EG: Equigranular Granite
BPG: Biotite Porphyritic Granite
GPG: Giant Porphyritic Granite
BRG: Biotite-bearing Red Granite
MRG: Muscovite-bearing Red Granite
CMC: Conlara Metamorphic Complex
PMC: Pringles Metamorphic Complex
REE deposit (Fenite)
PG
EG
32°30′
CMC
GPG
PMC
BPG
32°40′
BRG
MRG
0 4 8 Km
San Luis Province
Argentina
B
65°46′
65°45′
N
PG
EG
32°24′
Fenite
EG
32°25′
0 0.5 1 Km

Fig. 2

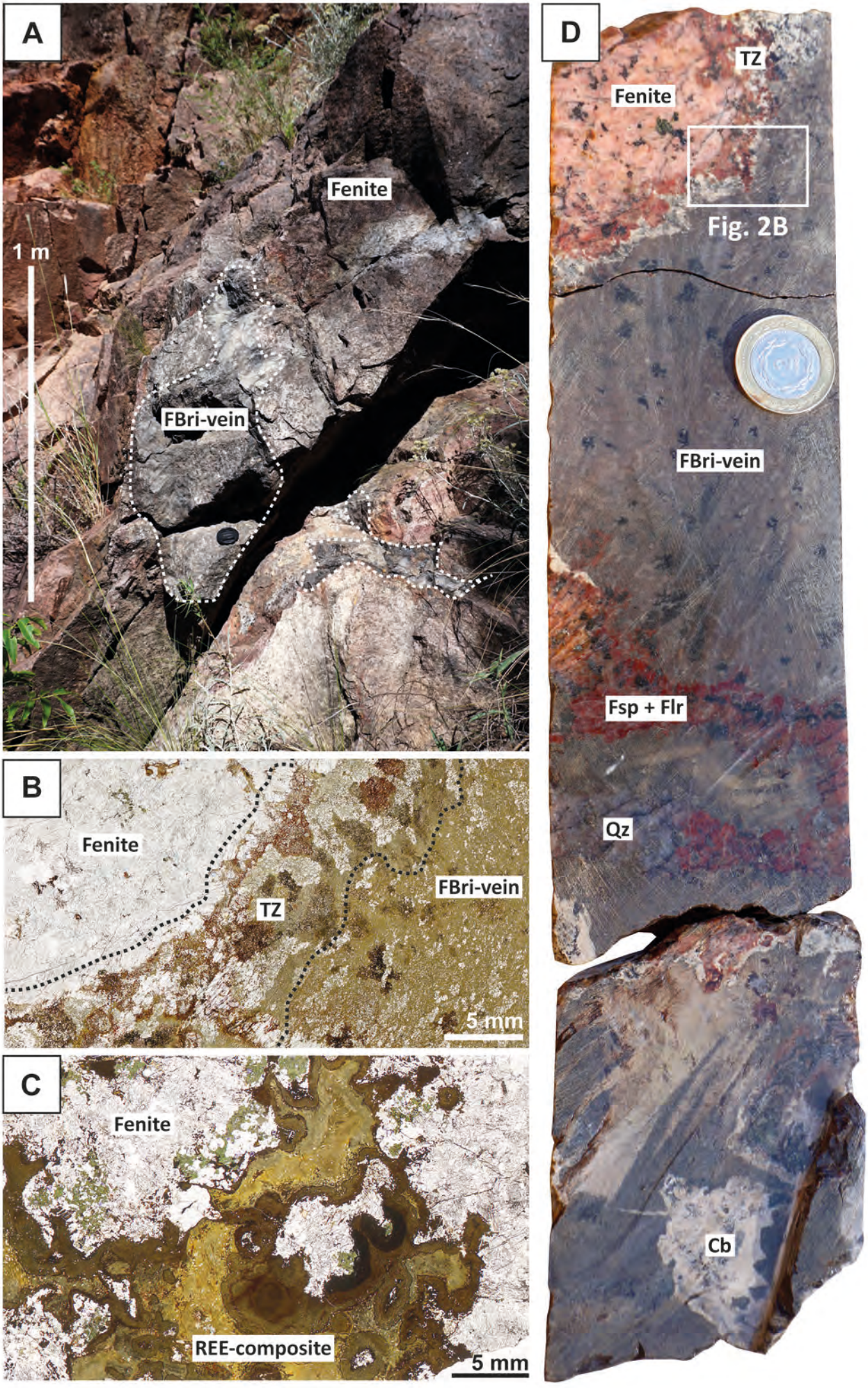
A
Fenite
1 m
FBri-vein
B
Fenite
TZ
FBri-vein
5 mm
C
Fenite
REE-composite
5 mm
D
TZ
Fenite
Fig. 2B
FBri-vein
Fsp + Flr
Qz
Cb

Fig. 3

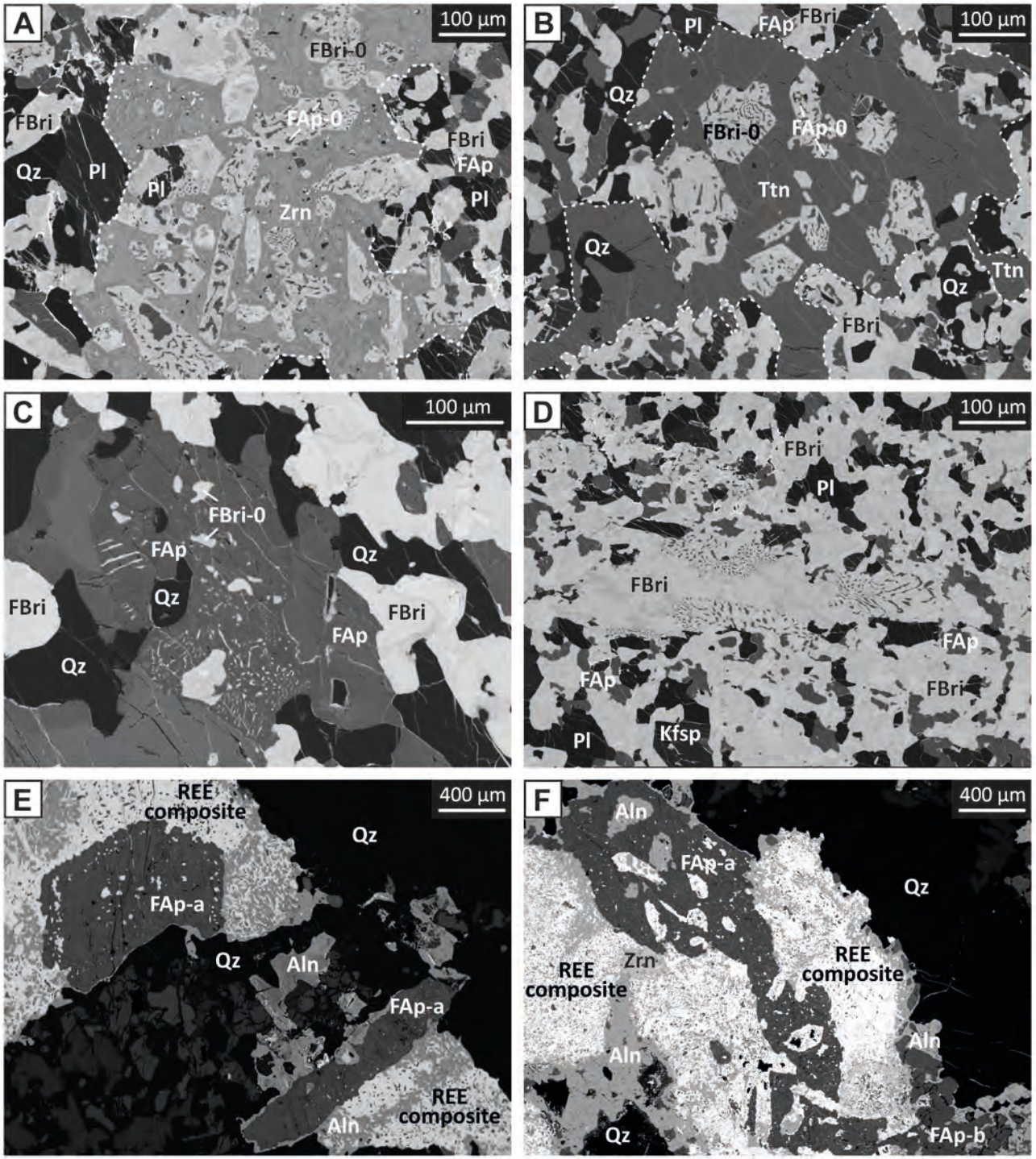
A
100 µm
FBri-0
FBri
FAp-0
FBri
FAp
Qz
Pl
Pl
Zrn
Pl
B
100 µm
Pl
FAp
FBri
Qz
FBri-0
FAp-0
Ttn
Qz
Ttn
Qz
FBri
C
100 µm
FBri-0
FAp
Qz
Qz
FBri
FBri
FAp
Qz
D
100 µm
FBri
Pl
FBri
FAp
FAp
FBri
Pl
Kfsp
E
400 µm
REE composite
Qz
FAp-a
Qz
Aln
FAp-a
Aln
REE composite
F
400 µm
Aln
FAp-a
Qz
Zrn
REE composite
REE composite
Aln
Aln
Qz
FAp-b

Fig. 4

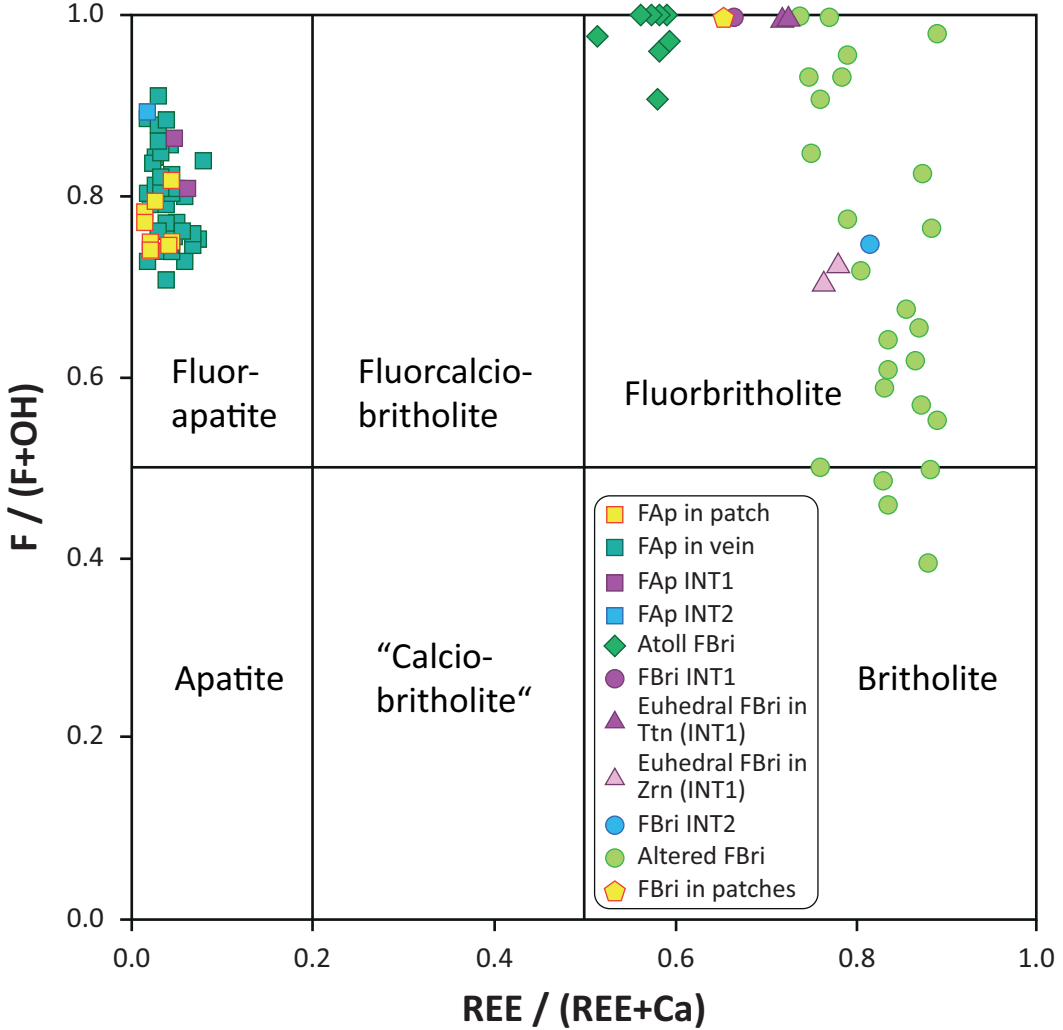
1.0
0.8
0.6
0.4
0.2
0.0
F / (F+OH)
0.0
0.2
0.4
0.6
0.8
1.0
REE / (REE+Ca)
Fluor-
apatite
Fluorcalcio-
britholite
Fluorbritholite
Apatite
“Calcio-
britholite“
Britholite
FAp in patch
FAp in vein
FAp INT1
FAp INT2
Atoll FBri
FBri INT1
Euhedral FBri in
Ttn (INT1)
Euhedral FBri in
Zrn (INT1)
FBri INT2
Altered FBri
FBri in patches

Fig 5

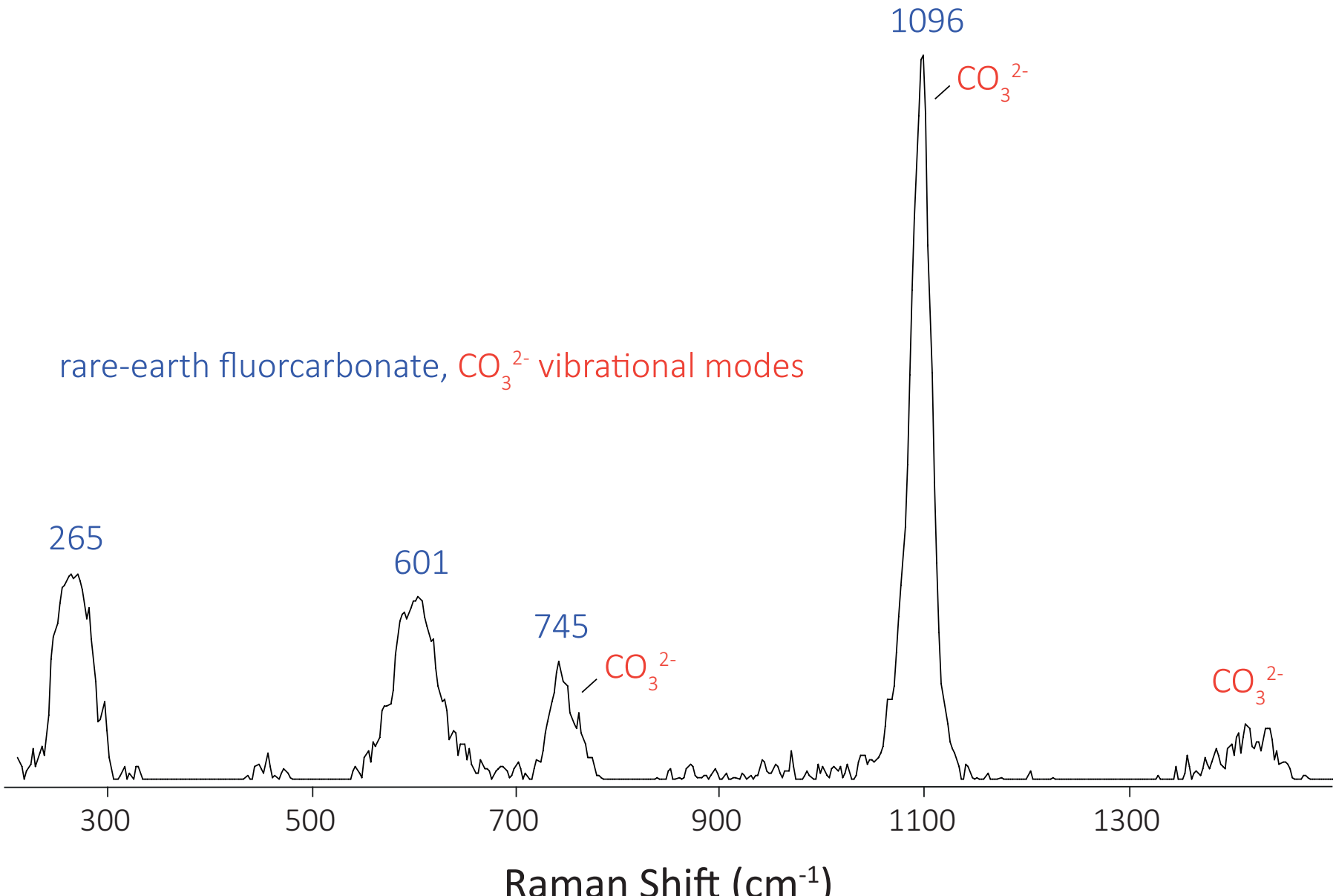
1096
CO_3^{2-}
rare-earth fluorcarbonate, CO_3^{2-} vibrational modes
265
601
745
CO_3^{2-}
CO_3^{2-}
300
500
700
900
1100
1300
Raman Shift (cm^{-1})

Fig.6

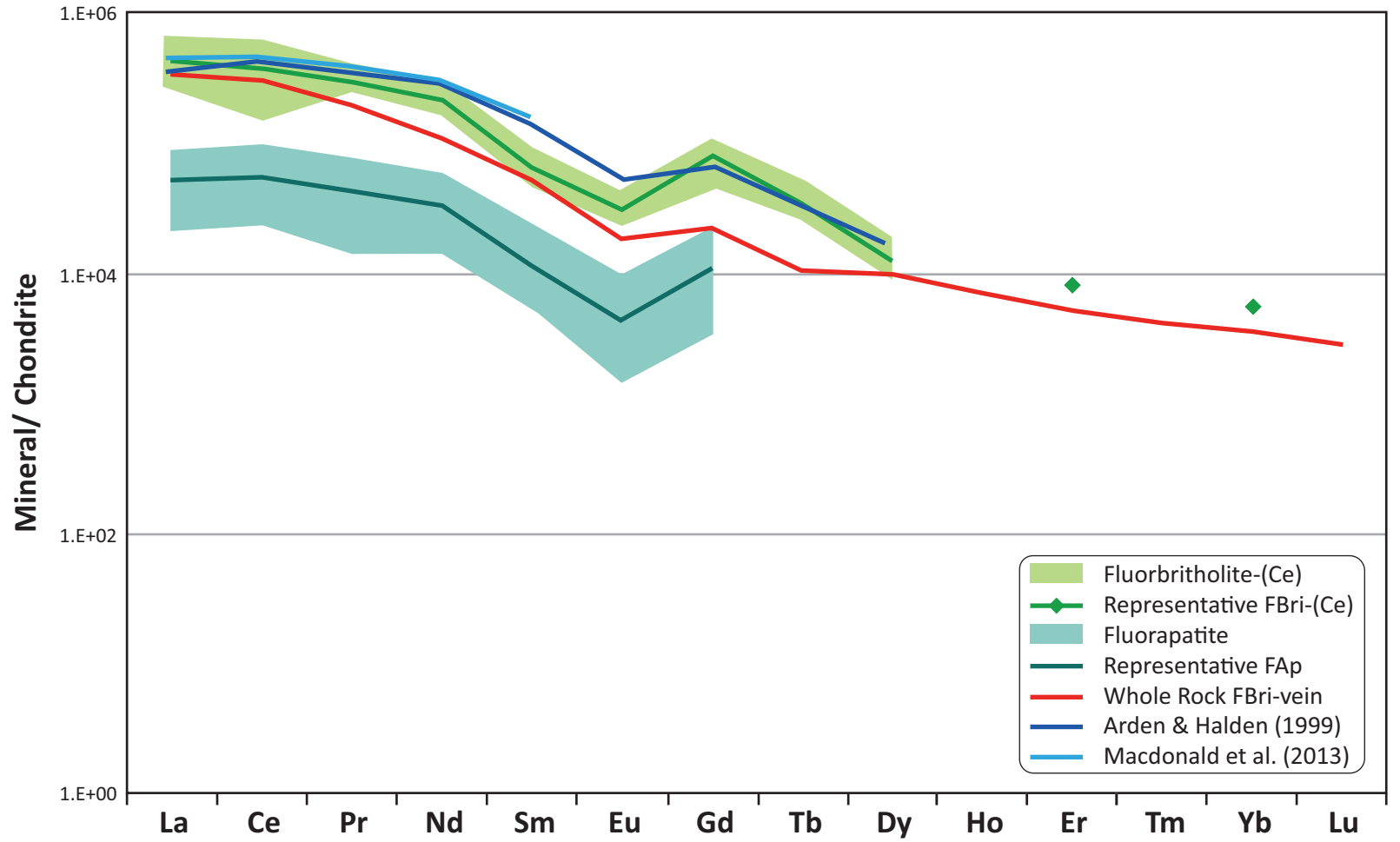
1.E+06
1.E+04
1.E+02
1.E+00
Mineral/ Chondrite
La
Ce
Pr
Nd
Sm
Eu
Gd
Tb
Dy
Ho
Er
Tm
Yb
Lu
Fluorbritholite-(Ce)
Representative FBri-(Ce)
Fluorapatite
Representative FAp
Whole Rock FBri-vein
Arden & Halden (1999)
Macdonald et al. (2013)

Fig. 7

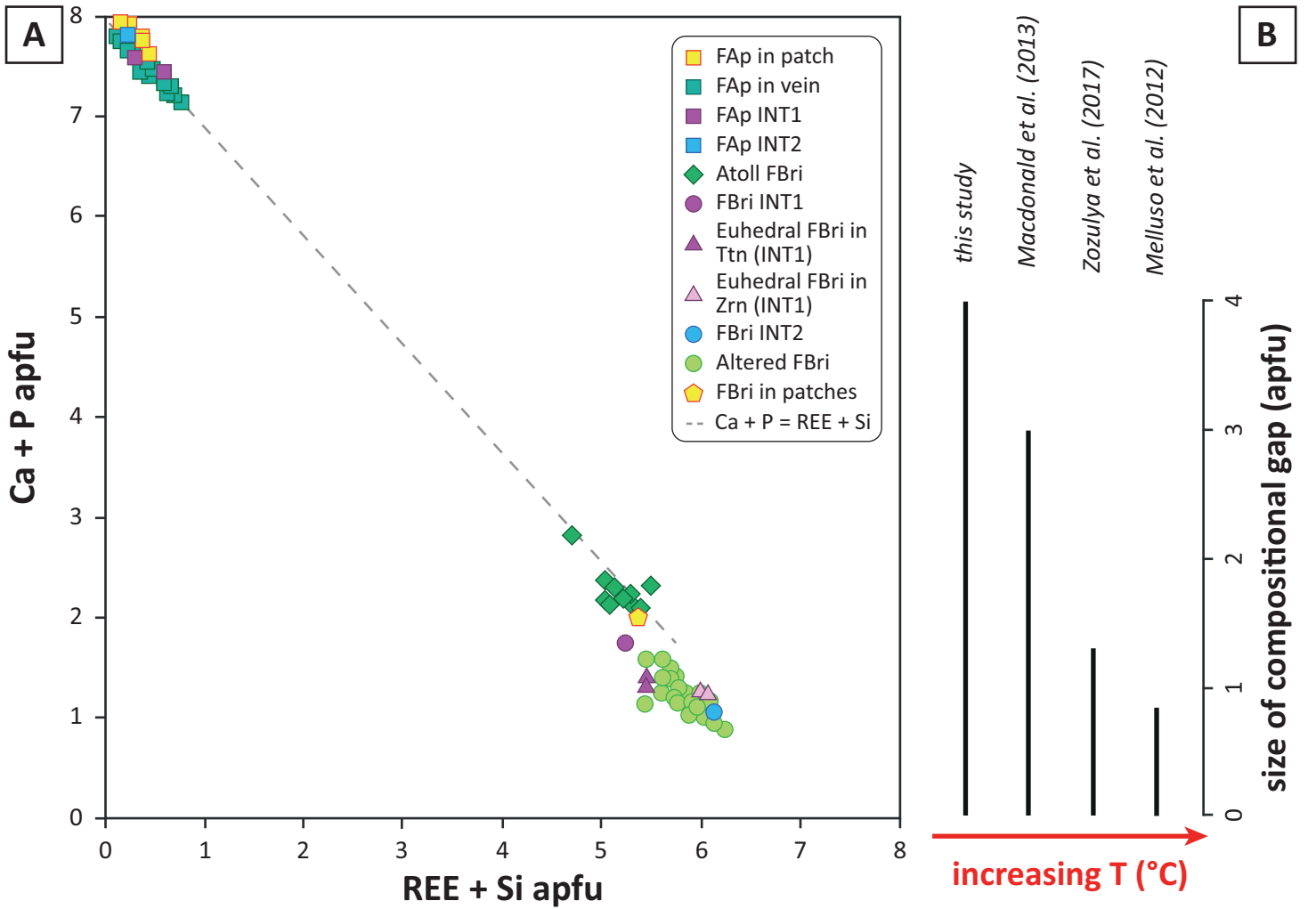
A
B
FAp in patch
FAp in vein
FAp INT1
FAp INT2
Atoll FBri
FBri INT1
Euhedral FBri in Ttn (INT1)
Euhedral FBri in Zrn (INT1)
FBri INT2
Altered FBri
FBri in patches
Ca + P = REE + Si
Ca + P apfu
REE + Si apfu
0
1
2
3
4
5
6
7
8
this study
Macdonald et al. (2013)
Zozulya et al. (2017)
Melluso et al. (2012)
increasing T (°C)
size of compositional gap (apfu)

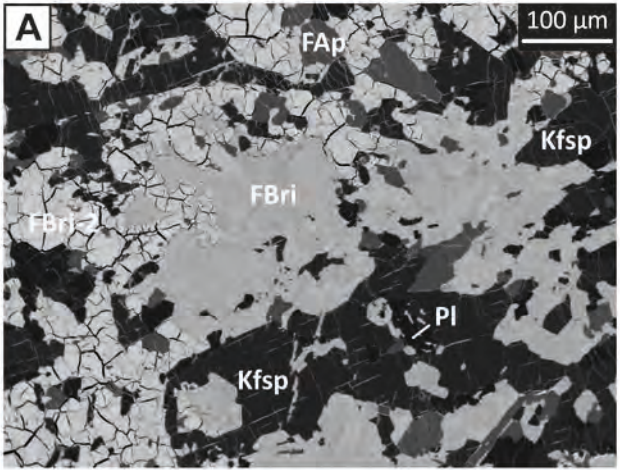
A
100 µm
FAp
Kfsp
FBri
FBri
Pl
Kfsp

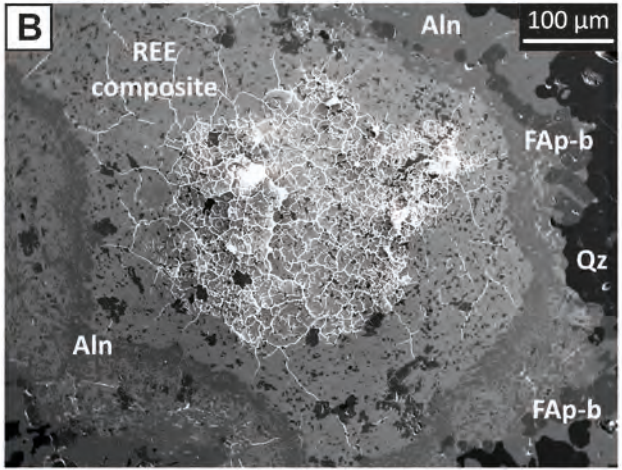
B
100 µm
Aln
REE
composite
FAp-b
Qz
Aln
FAp-b